Detecting a salt dome overhang with magnetotellurics: 3D inversion methodology and synthetic model studies

Anna Avdeeva[1], Dmitry Avdeev[2], and Marion Jegen[1]

ABSTRACT

Detecting a salt dome overhang is known to be problematic by seismic methods alone. We used magnetotellurics (MT) as a complementary method to seismics to investigate the detectability of a salt dome overhang. A comparison of MT responses for 3D synthetic salt models with and without overhang shows that MT is very sensitive to shallow salt structures and suggests that it should be possible to detect an overhang. To further investigate the resolution capability of MT for a salt dome overhang, we performed a 3D MT inversion study and investigated the impact of model parametrization and regularization. We showed that using the logarithms of the conductivities as model parameters is crucial for inverting data from resistive salt structures because, in this case, commonly used Tikhonov-type stabilizers work more equally for smoothing the resistive and conductive structures. The use of a logarithmic parametrization also accel-

erated the convergence and produced better inversion results. When the Laplace operator was used as a regularization functional, we still observed that the inversion algorithm allows spatial resistivity gradients. These spatial gradients are reduced if a regularization based on first derivatives in contrast to the Laplace operator is introduced. To demonstrate the favorable performance when logarithmic parametrization and gradient-based regularization are employed, we first inverted a data set simulated for a simple model of two adjacent blocks. Subsequently, we applied the code to a more realistic salt dome overhang detectability study. The results from the detectability study are encouraging and suggest that 3D MT inversion can be applied to decide whether the overhang is present in the shallow salt structure even in the case when only profile data are available. However, to resolve the overhang, a dense MT site coverage above the flanks of the salt dome is required.

INTRODUCTION

Imaging of offshore salt dome overhang structures that are associated with accumulations of oil and natural gas is a current challenge for the exploration industry and difficult to accomplish with seismic methods alone. Particularly, resolving salt boundaries on the steeply dipping flanks of such salt domes and the base of salt poses problems due to multiple reflections and mode conversions (Ogilvie and Purnell, 1996; Key et al., 2006).

The high contrast in electrical resistivity between the salt and the surrounding sediments provides an excellent target for magnetotelluric (MT) method and, therefore, MT can be regarded as a possible alternative or complementary method to explore salt dome overhangs (Hoversten et al., 2000). A number of recent studies have

investigated some aspects of imaging salt structures with MT (Constable et al., 1998; Hoversten et al., 1998, 2000; Key and Weiss, 2006; Zhdanov et al., 2009, among others). Most of these use 1D or 2D MT modeling or inversion for imaging salt structures. Zhdanov et al. (2009) present a fully 3D inversion algorithm, which they apply to marine MT data collected in the Gemini Prospect, Gulf of Mexico. They show that their code can map resistive structures like a salt dome with reasonable accuracy. In the current paper, we investigate the ability of 3D MT inversion to resolve the salt dome overhang.

A number of 3D MT inversion algorithms have been developed (Mackie and Madden, 1993; Newman and Alumbaugh, 2000; Zhdanov and Golubev, 2003; Sasaki, 2004; Siripunvaraporn et al., 2005; Avdeev and Avdeeva, 2009, among others). All of these

algorithms are designed to find models that fit the data and are geologically interpretable. Because 3D MT inversion is a large-scale problem, there are two main issues: the high memory requirements and large computational times. As in many other 3D MT codes, these issues are also addressed in our code $x3Di$ (Avdeev and Avdeeva, 2009). It is based on a limited-memory quasi-Newton (QN) optimization method Nocedal and Wright (1999). This method has become a popular tool to solve large-scale inverse problems (Newman and Boggs, 2004; Haber, 2005; Moorkamp et al., 2011, among others) because it requires only a few pairs of vectors to be stored in memory. Each pair of vectors consists of the vector of model parameters and the gradient of the objective functional at a previous iteration. Our experience shows that it is sufficient to keep information only from six previous iterations. To calculate the gradients of the objective functional efficiently, we use an adjoint approach (see Rodi, 1976). In this paper, we first remind the reader of the main aspects of the 3D MT inversion code. We then adjust the code to the specific problem of inverting for the geometry of a salt dome overhang by using the logarithms of the conductivities as model parameters and by introducing Gradient-based regularization. These modifications are necessary when one wants to resolve a resistive structure such as a salt dome. We demonstrate how these two modifications improve the convergence and the results of the inversion on a simplistic synthetic example consisting of two adjacent blocks. Finally, we apply the new improved code to investigate the detectability of a 3D salt dome overhang in a shallow marine environment. For this study, we construct two synthetic models based on an existing salt dome in the North Sea, one with and one without overhang. Using the 3D frequency domain integral equation code $x3D$ (Avdeev et al., 1997, 2002), we compare the responses obtained for these two salt dome models. We then invert these two data sets and assess the inversion results.

3D MT INVERSION

In this section, we first briefly review and then describe further improvements of our 3D MT inversion algorithm. Here, we mention only the aspects of the algorithm, which are essential for the paper. The reader can find more details in Avdeev and Avdeeva (2006); Avdeev and Avdeeva (2009).

The inversion code minimizes a classical Tikhonov-type regularized penalty function:

$$\varphi(\mathbf{m}, \lambda) = \varphi_d(\mathbf{m}) + \lambda \varphi_s(\mathbf{m}) \underset{\mathbf{m}, \lambda}{\rightarrow} \min, \qquad (1)$$

where

$$\varphi_d = \frac{1}{2} \sum_{i=1}^{N_S} \sum_{j=1}^{N_T} \beta_{ij} tr[(\mathbf{Z} - \mathbf{D})_{ij}^T (\mathbf{Z} - \mathbf{D})_{ij}] \qquad (2)$$

is a measure of the data misfit. Here, $\mathbf{m} = (m_1, \ldots, m_N)^T$ is a vector of model parameters, N is the number of model parameters to be recovered, N_S is the number of observation sites, N_T is the number of frequencies, and β_{ij} are positive weights calculated from the estimated data errors. The terms $\mathbf{Z}_{ij}$ and $\mathbf{D}_{ij}$ denote 2×2 complex-valued matrices of predicted and observed impedances, respectively.

The term $\lambda \varphi_s(\mathbf{m})$ in equation 1 is, as prescribed by regularization theory (see Tikhonov and Arsenin, 1977), a regularization part with a stabilizer φ_s and positive trade-off parameter λ. This stabilizer φ_s reduces the set of possible solutions. For example, if the stabilizer is based on the Laplace operator, i.e.,

$$\varphi_s = \sum_{k'=1}^{N} \left(\sum_{k=1}^{N} W_{k'k} m_k \right)^2, \qquad (3)$$

where $W_{k'k}$ is a finite-difference approximation of the Laplacian, solutions can only be models with minimum spatial variability or roughness.

When regularization is used in the inversion, we encounter an additional problem of finding the optimum trade-off parameter λ. We choose λ in a cooling manner similar to that of Haber et al. (2000). A relatively large value of λ is assigned initially and then reduced gradually. Each new problem is solved using the solution of the previous problem (i.e., the model obtained using the previous value of λ) as an initial guess. The choice of the initial value for λ and how fast it should be reduced is currently based on user experience. For the future, it would be desirable to develop some automated schemes.

To minimize φ, we employ a limited-memory quasi-Newton (QN) optimization method with simple bounds (see Nocedal and Wright, 1999). This optimization method requires a relatively small storage, which is proportional to $2 \times n_{cp} \times N$, where n_{cp} is the number of the correction pairs (practically, only a few). The correction pairs are the pairs of the vectors $\mathbf{m} = (m_1, \ldots, m_N)^T$ and $\mathbf{g} = (\frac{\partial \varphi}{\partial m_1}, \ldots, \frac{\partial \varphi}{\partial m_N})^T$ at few previous iterations. Many tests (not presented here) show that $n_{cp} = 6$ is usually enough and this is the number we are going to use for all the examples presented in this paper. Another advantage of the QN optimization method is that it requires calculation of gradients of the penalty function only, and requires no calculations of second-derivative terms. The calculation of gradients based on an adjoint approach is presented in Avdeev and Avdeeva (2009). The time needed to compute the gradient at a given period is equivalent to only two forward modelings (solution of a single forward and a single adjoint system of Maxwell's equations) and is independent of the number of model parameters. The forward and adjoint problems are solved with the integral equation (IE) forward-modeling code described in Avdeev et al. (1997, 2002). The same code is used to simulate 2×2 matrices $\mathbf{D}_{ij}$ of observed impedances for all synthetic tests presented in the paper.

To adapt the code for the specific problem of the salt dome overhang, we explore various parameterizations and regularization techniques. As we present below, these aspects of the inversion turn out to be very important when looking at resistive structures.

Model parameters

The model can be parameterized in resistivities $m_k = \rho_k$, conductivities $m_k = \sigma_k$, or some functions of ρ_k or σ_k. In the following, we compare inversion results for parametrization in terms of conductivities and logarithms of conductivities of the cells.

Model parameters — Conductivities

In Avdeev and Avdeeva (2009), we chose $m_k = \sigma_k$, $(k = 1, \ldots, N)$. Because the conductivities σ_k must be nonnegative

and realistic, the optimization problem of equations 1–3 has to be subjected to simple bounds

$$l_k < \sigma_k < u_k, \qquad (4)$$

where l_k and u_k are the lower and upper bounds, respectively, and $l_k \geq 0$.

To investigate how the MT inversion method works, when σ_k are the model parameters, we consider a model of two adjacent blocks. This model has been considered in various 3D forward-modeling and inversion papers (e.g., Wannamaker, 1991; Mackie et al., 1994; Avdeev et al., 1997; Siripunvaraporn et al., 2005; Avdeev and Avdeeva, 2009). The model consists of resistive and conductive adjacent blocks buried in a two-layered earth (see Figure 1). The inversion domain consists of $N_x \times N_y \times N_z = 20 \times 20 \times 9 = 3600$ rectangular cells with $dx = dy = 4$ km and reaches a depth of 32 km. Here, x, y, and z are pointing North, East and downward, respectively. The modeling domain coincides with the inversion domain. In an attempt to simulate a realistic field scenario, we cover the surface of the inversion domain with 80 randomly distributed MT sites, only requiring that MT sites do not occur in adjacent cells. The location of the sites and the numerical grid are also shown in Figure 1. It should be mentioned that the code poses no constraints on MT site locations. At these sites, we simulate data at frequencies of 10^3, 3.3×10^3, and 10^2 Hz ($N_T = 3$) and add 1% noise to the simulated data. As a starting model, we chose a uniform half-space of 50 Ωm ($m_k^{(0)} = 0.02$ S/m for $k = 1, \ldots, N$).

The first and fifth row in Figure 2 show the inversion result for nine different depth slices. The recovered image is very different from the true model and is not satisfactory, especially for the upper part of the model, where many artificial structures are visible. While reasonable resistivities are recovered for cells immediately underneath the MT sites, the resistivities of the other cells are poorly reconstructed leading to a "speckled" model.

Avdeev and Avdeeva (2009) investigate the reasons for the erratic resistivities in the upper part of the model and conclude that the standard Tikhonov regularization is not enough to provide consistently smooth underground structures. They implement an "additional regularization" to overcome the problem. In the model space $\mathbf{m} = (m_1, \ldots, m_N)$, they introduce a vector $\tilde{\mathbf{g}} = (\tilde{g}_1, \ldots, \tilde{g}_N)^T$ as

$$\tilde{\mathbf{g}} = \sum_{k'=1}^{N} f_{k'k} \frac{\partial \varphi}{\partial m_{k'}}, \qquad (5)$$

where

$$f_{k'k} = \begin{cases} \dfrac{e^{-\frac{1}{2}\left[\left(\frac{i'_x - i_x}{a_x}\right)^2 + \left(\frac{i'_y - i_y}{a_y}\right)^2\right]}}{\sum_{l_x=1}^{N_x} \sum_{l_y=1}^{N_y} e^{-\frac{1}{2}\left[\left(\frac{l_x - i_x}{a_x}\right)^2 + \left(\frac{l_y - i_y}{a_y}\right)^2\right]}}, & i_z = i'_z, \\ 0, & i_z \neq i'_z, \end{cases} \qquad (6)$$

and $k = \gamma(i_x, i_y, i_z)$, $k' = \gamma(i'_x, i'_y, i'_z)$, and $\gamma(i_x, i_y, i_z) = i_z + [i_y - 1 + (i_x - 1) \times N_y - 1] \times N_z$.

The vector $\tilde{\mathbf{g}}$ replaces the true gradient $\mathbf{g}$ of the objective function in the inversion. In this approach, two new parameters a_x and a_y are introduced and need to be chosen. We use a cooling approach for these parameters, similar to cooling of the regularization parameter λ. When such "additional regularization" is applied, the result is

greatly improved (see third and seventh row in Figure 2). To obtain this result, we start with $a_x = a_y = 3$ at the beginning of the inversion and slowly reduce it to $a_x = a_y = 1$ at the final inversion iterations. The resistivity and shape of conductive block is now very well recovered. The same is true for the resistive block, however, the recovered resistivity value (>200 Ωm) exceeds the true model resistivity (100 Ωm). This is due to the fact that when conductivities are used as model parameters, the stabilizer φ_s of equation 3 does not enforce smoothing on the resistive structures, because they have little impact on the overall value of the stabilizer. Therefore, if the target has a resistive character, a parametrization in terms of conductivities is not favorable. In the next section, we introduce the parametrization by logarithms of conductivities.

Logarithmic parameterization

The logarithmic parametrization is commonly used by inversion software developers (see, for example, Mackie and Madden, 1993; Newman and Alumbaugh, 2000), motivated by the fact that considering $\log(\sigma_k - l_k)$ or $\log[(\sigma_k - l_k)/(u_k - \sigma_k)]$ as unknown parameters, helps to keep the conductivities positive. Some advantages of the logarithmic parametrization also are discussed in Parker (1994). After such transformations, the bounds of the model parameters extend to infinity and the constrained problem of equations 1–4 turns
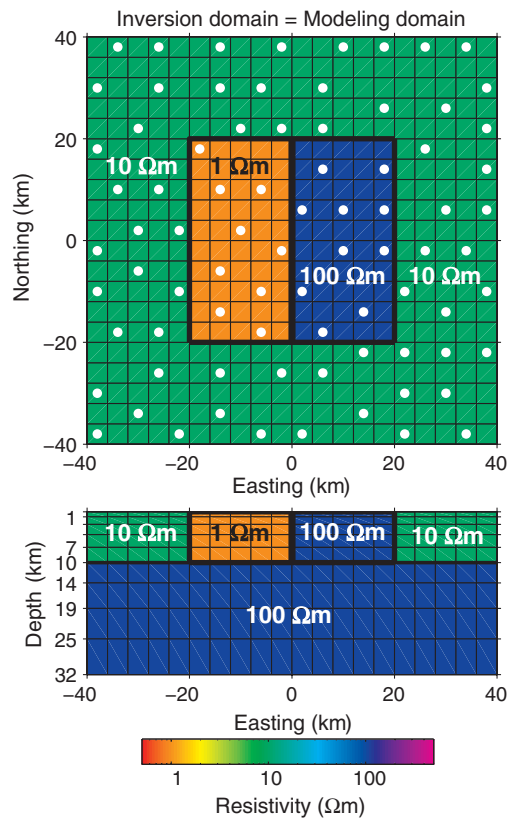

Figure 1. Two-block model used to test the inversion. The upper panel shows a horizontal slice through the top 10 km of the model. The lower panel presents the central vertical cross section through the model. Solid dots correspond to the locations of 80 randomly distributed MT sites used for synthetic tests. We also plot the numerical grid as solid black lines.

nominally to an easier unconstrained problem of equations 1–3. These transformations, however, can slow down the convergence of the inversion, if the solution is very close to the boundaries. For this reason, we do not include boundaries in the logarithmic transformation, but use $m_k = \log_{10}\sigma_k$ and still impose simple bound constraints as

$$\log_{10} l_k < \log_{10} \sigma_k < \log_{10} u_k. \tag{7}$$

Now, our optimization problem is defined by equations 1–3 and 7.

There are several advantages in using the logarithmic parametrization. First of all, in this case it does not matter what to invert for, conductivities or resistivities, because $\log_{10}\sigma_k$ is $-\log_{10}\rho_k$. Second, when a logarithmic parametrization is used, the stabilizer works more equally for smoothing resistive and conductive structures, while in case $m_k = \sigma_k$ the conductive structures are mostly the ones that are smoothed.

Inversion results for a logarithmic parametrization $m_k = \log_{10}\sigma_k$ with and without "additional regularization" are also shown in Figure 2. To obtain the result with the "additional regularization," we used the same values for the parameters a_x and a_y, as previously. It is always difficult to compare inversion results based on different model parametrizations or different types of regularization because each inversion has its own convergence path. To make this comparison, we choose models that produce a target data misfit φ_d of 0.04. The trade-off parameter λ is chosen and modified during the inversion in a way that produces the best result (note that we run the inversion with many different sequences of the parameter λ). To obtain the results presented in Figure 2, we start with $\lambda_{ini} = 10^8$ for $m_k = \sigma_k$ and with $\lambda_{ini} = 10^4$ for $m_k = \log_{10}\sigma_k$. When the logarithmic parametrization is employed the results are satisfactory even without the use of "additional regularization" (see second and sixth rows), the shape of both anomalies and the resistivity values are well resolved. There is still some erratic behavior at the top of the model, but in general, it is not as extreme as for the case of $m_k = \sigma_k$ (see first and fifth rows). When $m_k = \log_{10}\sigma_k$ and "additional regularization" is applied (see fourth and eights rows), the conductive and resistive blocks at the top of the model are nearly perfectly resolved, however, we observe very large resistivity values at the bottom. This can be explained by the fact that the regularization based on the Laplace operator allows the resistivity to have a constant spatial gradient. The effect of the choice of regularization on the result will be discussed later.

Figure 3 presents the convergence curves for all four inversions as a function of n_{fg}. The number n_{fg} increases by one after each evaluation of a pair φ and $\nabla_m\varphi$. This index is proportional to the time of the inversion and slightly larger than the number of QN iterations, due to possible additional calculations needed within the line search. The sequences of trade-off parameters λ used for the inversions are also shown as step functions in Figure 3. Using logarithmic parametrization not only improves the inversion
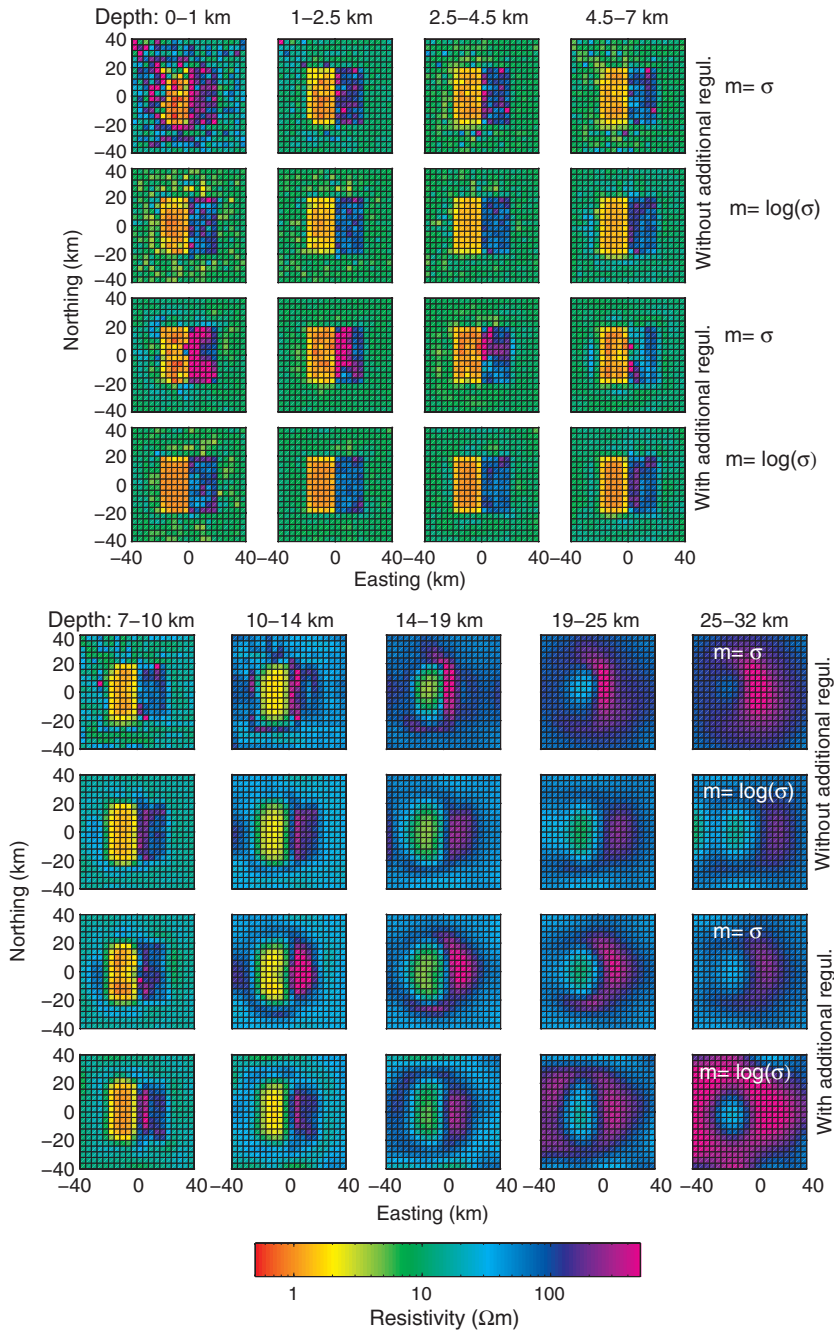

Figure 2. Comparison of the inversion results with different model parametrizations for the model presented in Figure 1. Nine horizontal slices through the models are presented. The first and fifth rows correspond to the inversion result without "additional regularization" using $\mathbf{m} = \boldsymbol{\sigma}$; the second and sixth rows correspond to the inversion without "additional regularization" and $\mathbf{m} = \log_{10}(\boldsymbol{\sigma})$; the third and seventh rows are the result of inversion with "additional regularization" and $\mathbf{m} = \boldsymbol{\sigma}$; the fourth and eighth rows — with "additional regularization" and $\mathbf{m} = \log_{10}(\boldsymbol{\sigma})$. Three frequencies and 80 MT sites were used in the inversions.

result, but also accelerates the convergence. We therefore use logarithmic parametrization together with the "additional regularization" for subsequent inversion experiments.

Regularization

Inversion results depend on the choice of the regularization functional φ_s. In this section, we compare the impact of two types of commonly used regularizations. As we mentioned in the previous section, the stabilizer based on the Laplace operator

$$\varphi_s^{\text{Laplace}} \approx dxdy \sum_{\alpha\beta\gamma} \left[\frac{\partial^2 m}{\partial x^2} + \frac{\partial^2 m}{\partial y^2} + \frac{\partial^2 m}{\partial z^2} \right]^2_{\alpha\beta\gamma} dz_\gamma \qquad (8)$$

allows the resistivity to have constant spatial gradients, which can produce very high resistivity values. This issue can be resolved with a stabilizer based on the following finite-difference approximation to the Gradient

$$\varphi_s^{\text{Gradient}} \approx dxdy \sum_{\alpha\beta\gamma} \left[\left(\frac{\partial m}{\partial x}\right)^2 + \left(\frac{\partial m}{\partial y}\right)^2 + \left(\frac{\partial m}{\partial z}\right)^2 \right]_{\alpha\beta\gamma} dz_\gamma. \qquad (9)$$

These two types of regularizations produce very similar results (see Figures 4 and 5). However, excessively high resistivity values at the bottom of the model disappear when Gradient-based regularization of equation 9 is applied. It should be mentioned that Figure 5.06b of Parker (1994) also presents a comparison of Laplace and Gradient-based regularization, however, only for a 1D case. He shows that solutions agree remarkably well in conductive regions, whereas for the resistive parts the solution based on Laplace regularization is an order of magnitude more resistive in some places, which further confirms our conclusions.

It is difficult to compare the inversions when different regularization techniques are applied because we have to choose different optimum sequences of trade-off parameters λ. In an attempt to have two comparable inversions, we use the following strategy for choosing the initial value λ_{ini} for the trade-off parameter. We start the inversions with a uniform half-space model, where the stabilizer $\varphi_s = 0$. After one iteration of the inversion with Laplace-based regularization, we obtain the model $\mathbf{m}^{(1)}$ and a nonzero value of $\varphi_s^{\text{Laplace}}(\mathbf{m}^{(1)})$. For this model, we calculate the Gradient-based stabilizer $\varphi_s^{\text{Gradient}}(\mathbf{m}^{(1)})$ and choose initial values of trade-off parameters such that

$$\lambda_{ini}^{\text{Laplace}} \varphi_s^{\text{Laplace}}(\mathbf{m}^{(1)}) = \lambda_{ini}^{\text{Gradient}} \varphi_s^{\text{Gradient}}(\mathbf{m}^{(1)}). \qquad (10)$$

For the inversion results in Figures 4 and 5, initial trade-off parameters are $\lambda_{ini}^{\text{Laplace}} = 10^4$ and $\lambda_{ini}^{\text{Gradient}} = 6 \times 10^{-3}$. After the initial trade-off parameter is chosen, we start the inversion and decrease the trade-off parameter every time the convergence slows down significantly. The cooling rate of parameter λ has to be chosen by the user. Our experience shows that slow cooling of the parameter produces better results.

The comparison of the inversion convergence rates for Laplace-based and Gradient-based regularizations is presented in Figure 6. The convergence curves are similar for both regularization techniques and the program takes between 10 and 15 hours to reach the target value of data misfit φ_d (one $n_{\text{fg}} \approx$ two min on an Intel Core2 Duo CPU, T9300 @ 2.50 GHz, 1.98 Gb of RAM Laptop).

Now that we have demonstrated the basic properties of possible model parametrizations and regularization terms on a simple test model, we will examine how far we can use MT inversion to recover the geometry of a salt dome structure and, in particular, whether we can resolve the existence of an overhang at its flanks. As we showed that $m_k = \log \sigma_k$ as model parameters and a Gradient-based stabilizer together with "additional regularization" are the optimum choices, these are the inversion settings we use in the following.

SALT DOME OVERHANG DETECTABILITY STUDY

In this study, we examine and compare two salt dome models (see Figure 7), based on an existing salt dome located in a tidal area of the North Sea. The models consist of a layered background and two resistive salt dome structures with a resistivity of 125 Ωm. The difference between these two models is the presence of a 1 km thick and 1 km wide overhang in the larger salt structure in one of the models. Our main focus lies on investigating the effect of the overhang of the large salt structure onto the MT responses. The smaller salt structure has been included to test whether the signal of two adjacent salt domes can be differentiated. The depth to the top of the larger salt structure is 50 m and to the smaller one 1200 m below a shallow sea of 2 m thickness. The lengths of the larger and smaller anomalies are 60 and 14 km, respectively. The salt domes originate from a 1 km thick horizontal salt layer at a depth of 6.2 km.

3D forward modeling

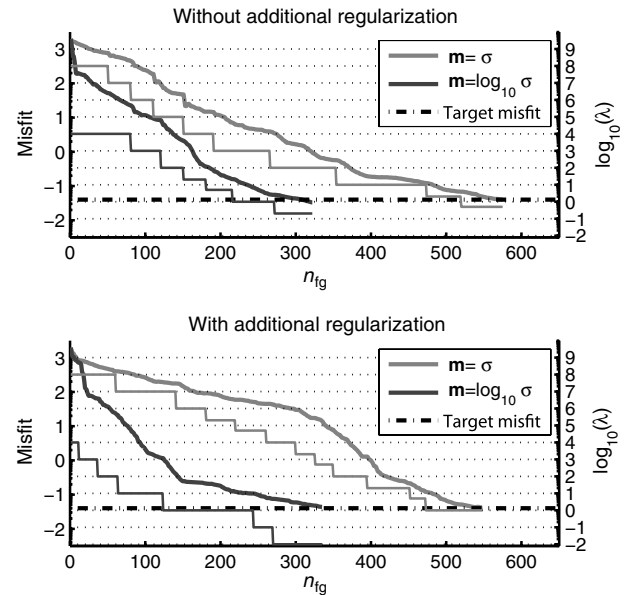For the feasibility study, we first perform a number of forward modelings using the 3D IE frequency-domain code. For

Figure 3. Convergence curves for the inversions with two types of model parameters: $\mathbf{m} = \boldsymbol{\sigma}$ (grey) and $\mathbf{m} = \log_{10}(\boldsymbol{\sigma})$ (black). The regularization parameters λ are also shown as a step functions in the same colors. The upper panel corresponds to the inversion results when no "additional regularization" is applied and the lower panel to inversion results with "additional regularization".

the numerical modeling, the volume has to be discretized into prisms, where we assume that all prisms in the mesh have the same horizontal area $dx \times dy$, but their vertical size dz_k may vary with depth. In our case, the modeling domain comprises $N_x \times N_y \times N_z = 320 \times 160 \times 13$ rectangular prisms, with $dx = dy = 250$ m, and extends to 7.2 km depth.

We simulate magnetotelluric (MT) data for 22 frequencies in the range from 100 to 10^{-5} Hz. To test the sensitivity of the MT responses to the salt structures, we calculate a 3D effect defined as

$$R_{\text{salt}}^{m_1} = \frac{|Z_{xx}^{m1} - Z_{xx}^{\text{back}}|^2 + |Z_{xy}^{m1} - Z_{xy}^{\text{back}}|^2 + |Z_{yx}^{m1} - Z_{yx}^{\text{back}}|^2 + |Z_{yy}^{m1} - Z_{yy}^{\text{back}}|^2}{|Z_{xx}^{\text{back}}|^2 + |Z_{xy}^{\text{back}}|^2 + |Z_{yx}^{\text{back}}|^2 + |Z_{yy}^{\text{back}}|^2}$$

(11)

at the sites located at the sea floor and with (x, y) coordinates coinciding with the center of each cell. In equation 11, Z_{xx}^{m1}, Z_{xy}^{m1}, Z_{yx}^{m1}, and Z_{yy}^{m1} are the complex-valued entries of the impedance tensor for the model without overhang (model 1 in Figure 7); Z_{xx}^{back},

Z_{xy}^{back}, Z_{yx}^{back}, and Z_{yy}^{back} are the impedance tensor entries for the 1D layered background. This 3D effect for five frequencies is shown in Figure 8 and reveals MT is particularly sensitive to the shallow salt structure. This can be explained by the fact that the electric currents are squeezing in the narrow conductive area above the resistive salt dome. The deformation of the electric field lines is the largest for the shallow salt dome. Another conclusion that can be drawn from Figure 8 is that the effect of the salt structures is very localized. The shape of the 3D response is approximately following the outline of the anomaly. Hence, the smaller salt structure should not affect an electromagnetic measurements above the larger one.

To investigate the effect of the presence of the salt dome overhang, we compare the responses from the models with and without overhang. To do this, we calculate the residuals

$$R_{\text{overhang}} = \frac{|Z_{xx}^{m2} - Z_{xx}^{m1}|^2 + |Z_{xy}^{m2} - Z_{xy}^{m1}|^2 + |Z_{yx}^{m2} - Z_{yx}^{m1}|^2 + |Z_{yy}^{m2} - Z_{yy}^{m1}|^2}{|Z_{xx}^{m1}|^2 + |Z_{xy}^{m1}|^2 + |Z_{yx}^{m1}|^2 + |Z_{yy}^{m1}|^2}$$

(12)

Figure 4. Comparison of the inversion results with Laplace and gradient based regularizations. Nine horizontal slices through the models are presented. The first and fourth rows correspond to the inversion result when the regularization functional φ_s is based on the Laplace operator (equation 8); for the second and fifth rows φ_s is based on the first derivatives (equation 9); the third and sixth rows show the true model. "Additional regularization" and logarithmic model parameters $\mathbf{m} = \log_{10}(\boldsymbol{\sigma})$ were employed to obtain both results. Three frequencies and 80 MT sites were used in the inversions.
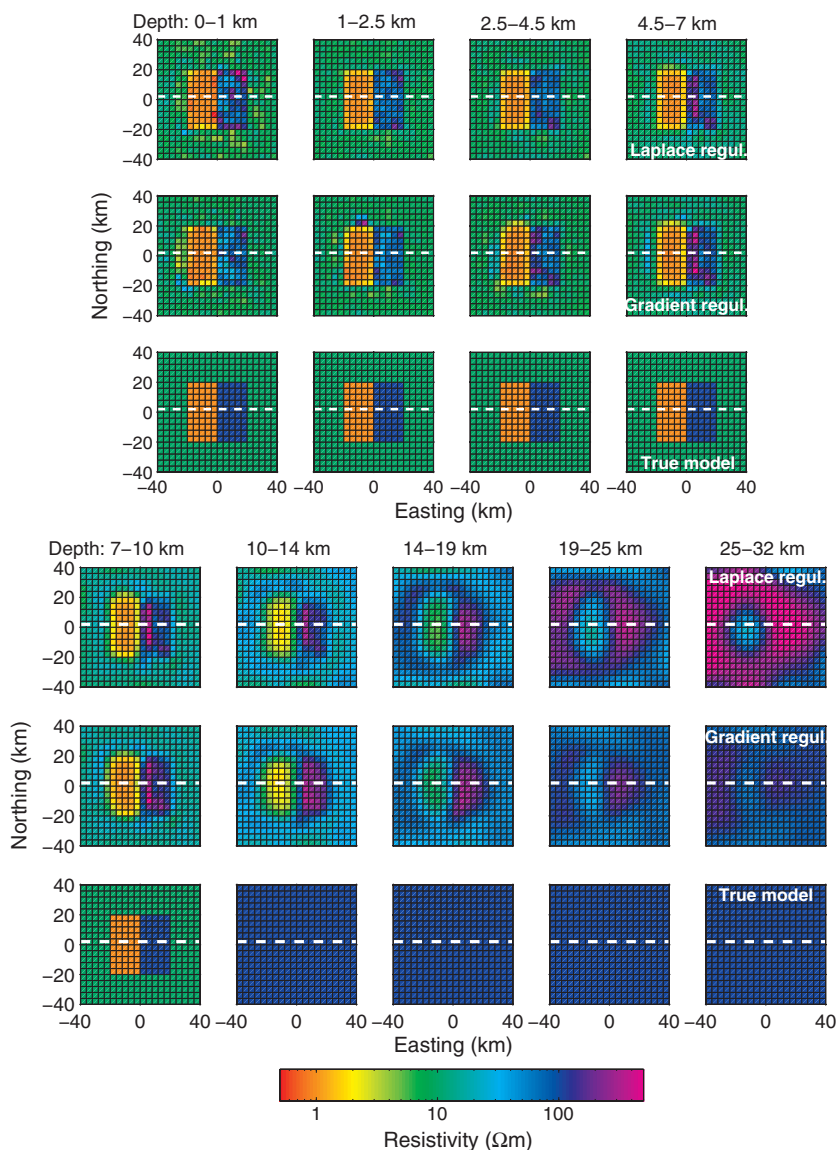
again at the sites located at the sea floor and with (x, y) coordinates coinciding with the centers of all the cells. The superscripts $m1$ and $m2$ stand for models without and with overhang, respectively. The residuals for five of the 22 frequencies are shown in Figure 9. The effect of the overhang is very localized and particularly strong for frequencies between 0.1 and 0.001 Hz. To show the effect of the overhang in more detail and to visualize how local this effect is, we also plot the apparent resistivity and phase curves for a frequency of 0.1 Hz along the profile crossing the left side of the large salt structure, $y \in [-12, -6]$ km and $x = -23.5$ km (see Figure 10). We omit the diagonal elements in the figure because they are a few orders of magnitude smaller than the off-diagonal ones and are not particularly useful for resolving the anomaly. From the above comparisons, we conclude that it is possible to see the presence of the overhang, but it is vital to have MT sites just above it. In other words, the MT site coverage should be denser on the sides of the salt structure.

In the following, we investigate how the resolution changes with depth to the top of the salt structure and also with the lateral extent of the overhang. We use a set of models similar to the salt models considered earlier, but with the top of the salt located deeper, at 275 m and 725 m below the sea floor, respectively. The vertical cross sections through these models are presented in Figure 11. We only show the part around the large salt structure because the rest of the modeling domain stays exactly the same as in the previous examples. We again compute the responses for all these models at the sea floor and in every cell of the modeling domain. The 3D effect R_{salt} from equation 11 for these models looks very similar to the 3D effect shown in Figure 8, nearly copying the shape of the salt structure and is, therefore, not presented here. The main difference is that the maximum sensitivity is shifted to lower frequencies. For model three, we only start to sense the anomaly ($R_{\text{salt}} > 0.1$) for a frequency of 1 Hz, whereas for model six, we sense it at 0.1 Hz. Another difference is that the overall sensitivity decreases when the top of the salt shifts deeper. For the previous example, when the top of the salt is 50 m below the sea floor, the maximum sensitivity $R_{\text{salt}}^{m_1}$ is 70, while the maxima are $R_{\text{salt}}^{m_3} = 10$ and $R_{\text{salt}}^{m_6} = 1.5$ for model three and model six, respectively. These numbers mean that it is still easy to resolve the anomaly as a whole.

With respect to the detectability of the overhang, the situation has changed. As expected, it is much more difficult to resolve the overhang when the top of the salt structure is deeper. In Figures 12 and 13, we show the apparent resistivity and phase curves for all models presented in Figure 11. In these figures, the vertical scale is not the same, but it is adjusted to make it possible to distinguish between the curves. In all cases, the ρ_{yx}^{app} component contributes the most to the detectability of the overhang. When the top of the salt is at 275 m depth below the sea floor, the maximum relative difference in ρ_{yx}^{app} between models with and without overhang is 28% and 44% for 1 and 2 km wide overhang, respectively. When the top of the salt is deeper at 725 m below the sea, these numbers decrease to 12% and 23% for 1 and 2 km wide overhang, respectively. Increasing the width of the overhang not only widens the region where one can identify the overhang, but also the difference between the curves becomes larger. From these figures, we conclude that it should be possible to distinguish between the models with and without overhang when the top of the salt is 275 m below the sea floor, especially for the 2 km wide overhang.
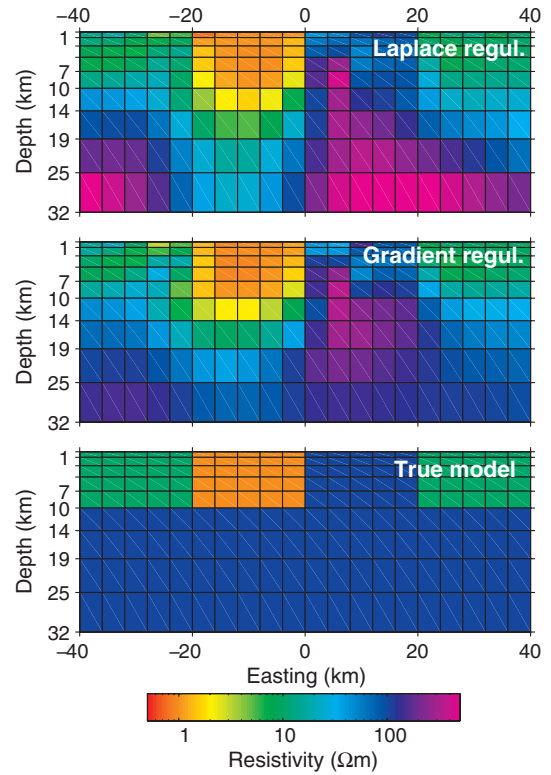

Figure 5. Comparison of the inversion results with Laplace and gradient based regularizations for a vertical cross section through the models. The location of the cross section is shown as a dotted white line in Figure 4. The upper panel presents the inversion result when the regularization functional φ_s is based on the Laplace operator (equation 8); for the middle panel φ_s is based on the first derivatives (equation 9); the lower panel shows the true model. "Additional regularization" and logarithmic model parameters $\mathbf{m} = \log_{10}(\boldsymbol{\sigma})$ were employed to obtain both results. Three frequencies and 80 MT sites were used in the inversions.
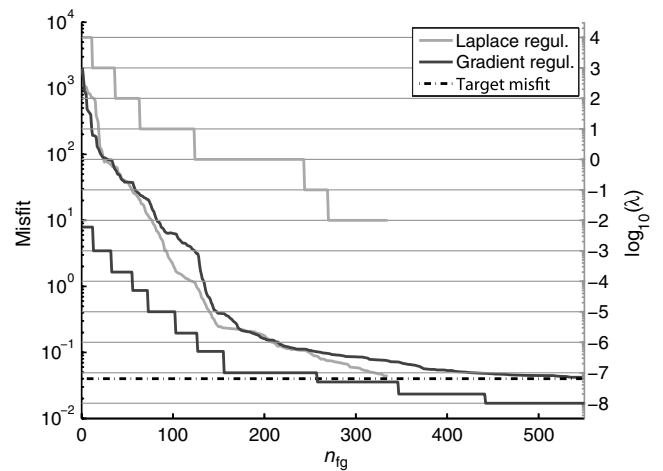

Figure 6. Comparison of the convergence curves for inversions with the regularization functional φ_s based on the Laplace operator (light gray line) and with φ_s based on the first derivatives (dark gray line). The regularization parameters λ are also shown as a step functions in the same colors. "Additional regularization" and logarithmic model parameters $\mathbf{m} = \log_{10}(\boldsymbol{\sigma})$ were employed to obtain both results.

Avdeeva et al.

Figure 7. Synthetic models based on a salt structure in the North Sea. The left two panels depict vertical cross sections through models without overhang (upper panel) and with overhang (lower panel). The right panel shows the horizontal cross section at a depth of 1300 m below the sea floor through the model without overhang. Black lines on the panels show the inversion domain. Red lines on the right panel indicate the positions of three MT profiles used for some of our inversion runs (see section "3D inversion of the salt dome data" in this paper).
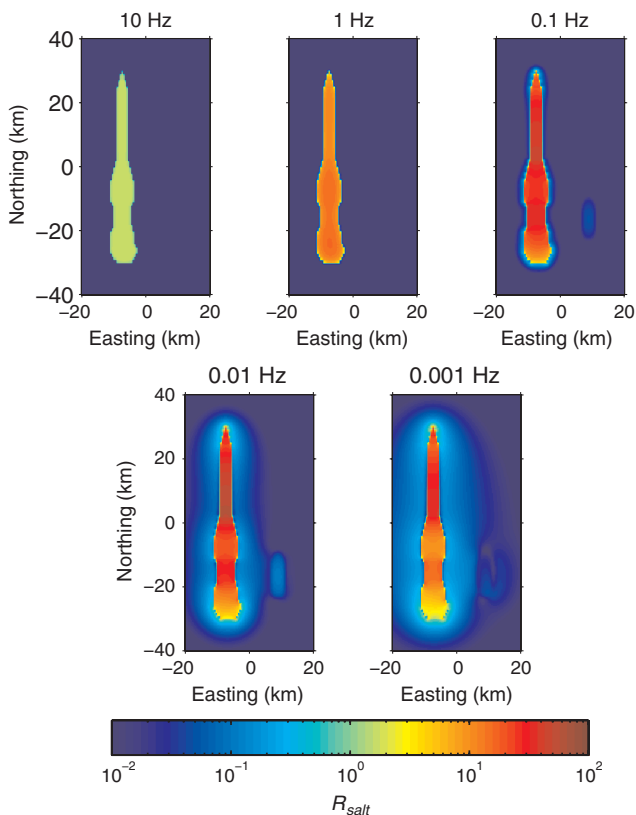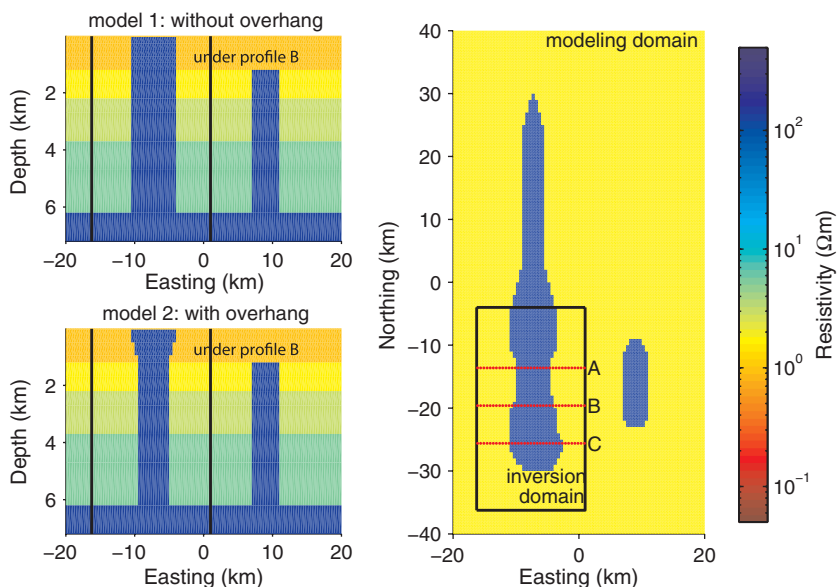
Figure 8. Normalized difference between the MT response of the resistive salt structure without overhang and the MT response of the 1D background model (equation 11). Each slice corresponds to the normalized difference at a single frequency, given above each panel.
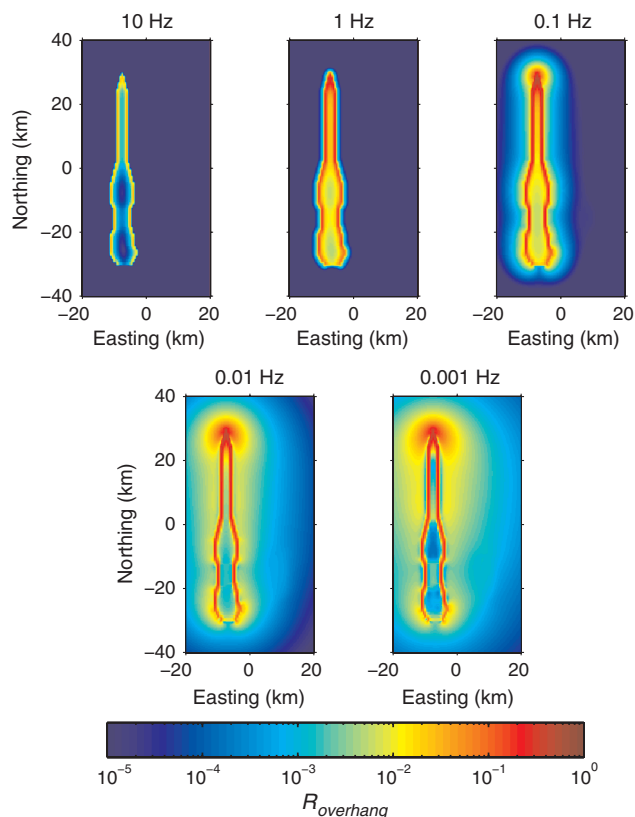
Figure 9. The effect of the presence of the overhang in the salt structure with respect to the model without overhang derived from the MT responses (equation 12). Each slice corresponds to the effect for a single frequency denoted above each panel.

When the top of the salt is 725 m deep, it is not possible to resolve a 1 km wide overhang and an overhang with a width of 2 km may only be resolved with marine magnetotelluric data of above average quality.

In the next section, we investigate how well the models of the salt dome with and without overhang can be recovered by our 3D MT inversion algorithm, in the best case scenario (models one and two).
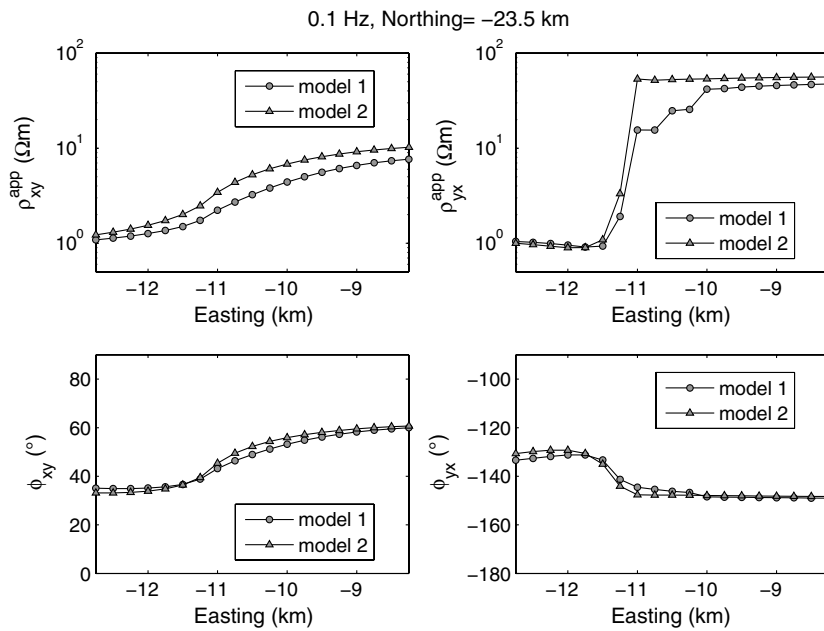

Figure 10. Comparison of sea floor apparent resistivities and phases across the side of the salt structures. Circles and triangular show the responses at 0.1 Hz for models without and with overhang, respectively (model one and model two of Figure 7).
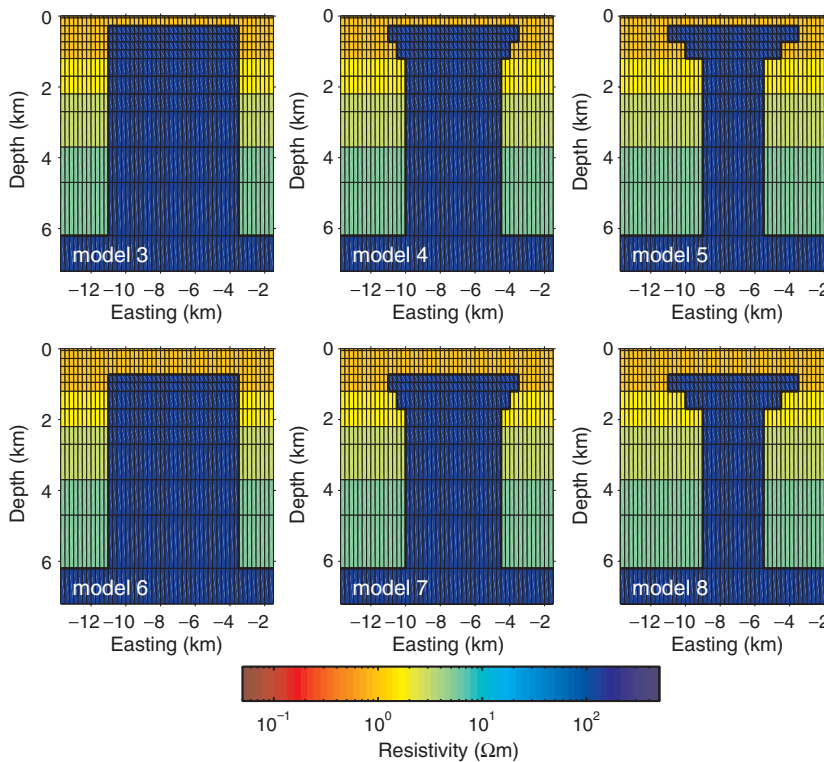
Figure 11. Synthetic models based on a salt structure in the North Sea. The first row presents the models where the top of the salt is located 275 m below the sea floor. For the second row, the depth to the top of the salt structure is 725 m. The left two panels show the models without overhang, while at the middle and right panels the models have a 1 km thick overhang with width of 1 and 2 km, respectively.

3D inversion of the salt dome data

For the 3D inversion study, we use subsets of data from salt dome models with and without overhang at five out of 22 frequencies (10, 1, 0.1, 0.01, and 0.001 Hz) that has been presented in the previous section. Our experience from previous synthetic studies shows that it is enough to use only five frequencies for this experiment. To simulate these observed data, the modeling domain consisted of $320 \times 160 \times 13$ prisms. We add 5% random noise to the simulated

data and use an 11 Ωm half-space model as an initial guess for all subsequent inversion runs.

To reduce the computation time and to create a more realistic scenario, for the inversion we choose a smaller, coinciding modeling and inversion domain of $N = N_x \times N_y \times N_z = 129 \times 69 \times 13 = 115,713$ rectangular prisms, with $dx = dy = 250$ m that only covers a part of the large salt structures (see black rectangle in Figure 7). Horizontal and vertical slices through the inversion

Figure 12. Comparison of sea floor apparent resistivities and phases across the side of the salt structures. The top of the salt structures is located 275 m below the sea floor. Circles, triangular, and squares show the responses at 0.01 Hz for models without, with 1 and 2 km wide overhang, respectively (models three, four, and five in Figure 11).
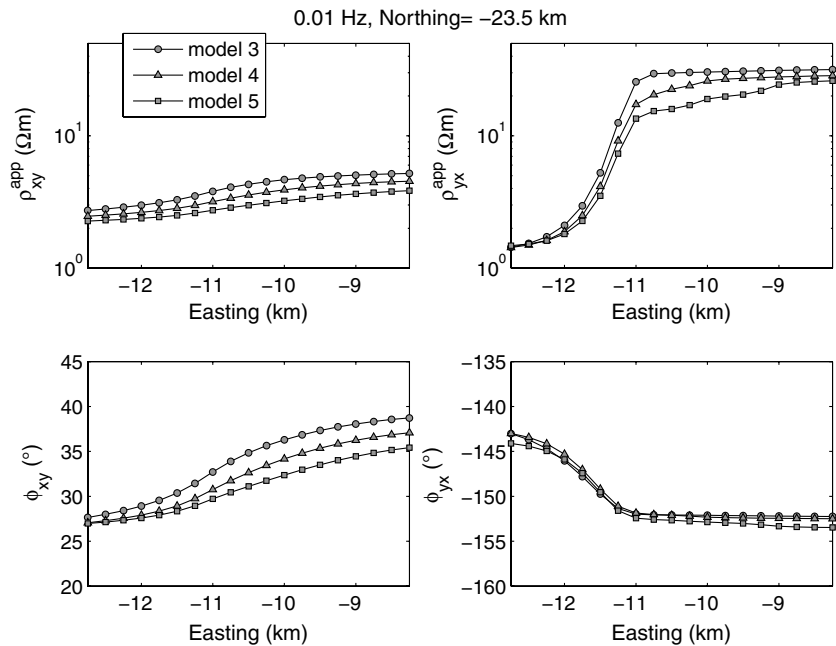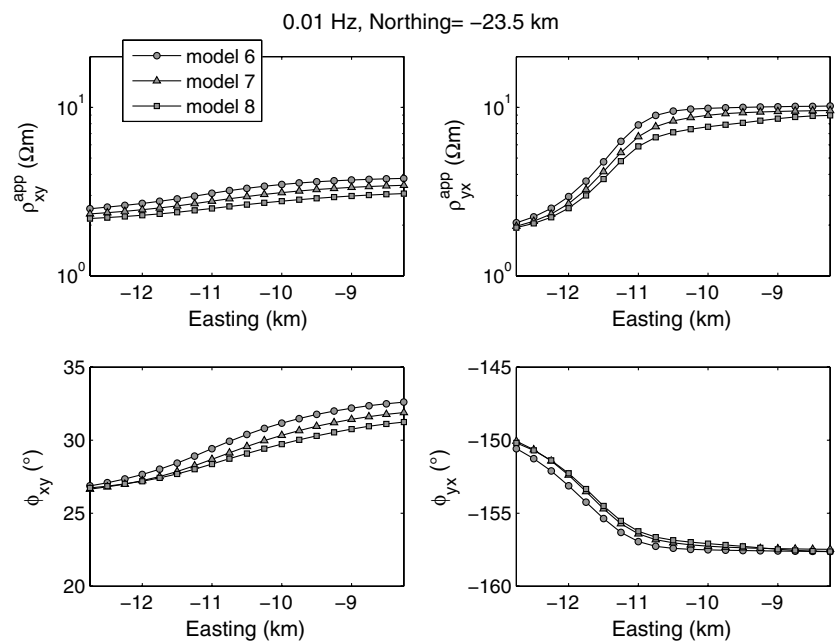

Figure 13. Comparison of sea floor apparent resistivities and phases across the side of the salt structures. The top of the salt structures is located 725 m below the sea floor. Circles, triangular, and squares show the responses at 0.01 Hz for without, with 1 and 2 km wide overhang, respectively (models six, seven, and eight in Figure 11).

results are shown in Figures 14, 15, 16, and 17. In an attempt to improve these results, we add two more frequencies per decade and continue to run the inversion. However, the value of data misfit is nearly the same whether five or 13 frequencies are used and no improvement is achieved.

In our first experiment with these salt dome models (Figures 14 and 15), we use a subset of 1995 sea floor MT sites with 500 m spacing. All sites are positioned inside the black dashed rectangle in Figure 14, covering part of the inversion domain. The 3D IE forward modeling code requires a layered background everywhere outside the modeling domain. Hence, the responses near the edge where the true salt dome structure extends outside the modeling/inversion domain cannot match the simulated data, and the true resistivity values near this edge can not be recovered. This effect is strongly reduced about 5 km from that edge and we obtain good results throughout the rest of the inversion domain. Inversion runs based on 5 and 200 Ωm half-spaces initial models deliver similar results (not shown here). The inversion of these data demonstrates that the salt structure can be resolved (see Figure 14). A distinction between models with and without overhang is possible closer to the end of the salt structure (Profile C) and it becomes more and more difficult to distinguish the overhang when we move away from this edge (see Figure 15).

Because the coverage by 1995 MT sites is not feasible in reality, we also study the effect of sparser coverage. We use data along three profiles crossing the salt structures (see Figure 7). Each profile consists of 35 equally spaced MT sites. The distance between adjacent sites is now 500 m and the distance between profiles is 6 km. Large distances (6 km) between the profiles enforces a need for a strong regularization along the salt structure (along x axis). Accordingly, we chose values of $a_x = 8$ and $a_y = 3$ in the "additional regularization" of equations 5 and 6.

Figures 16 presents horizontal slices through the inversion result for model without overhang. For this inversion, we again used an 11 Ωm half-space as a starting model. From this figure one can see that reasonable resistivity values are recovered immediately below the MT sites and at ≈1 km lateral distance from the profiles.

Figure 17 shows three vertical cross sections through the resulting inversion models without and with overhang (left and right panels, respectively). The cross sections presented are just beneath the profiles A, B, and C. Comparing the recovered image with the true model, we see that the shape and the position of the resistive
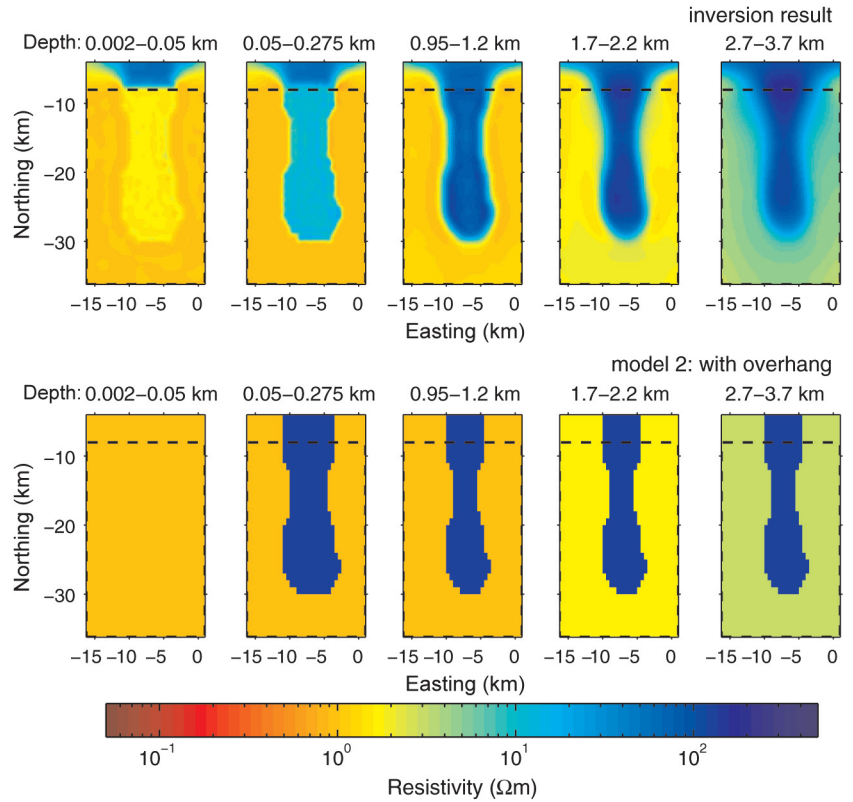

Figure 14. Comparison of the 3D inversion result (upper row) to the true model (lower row) of the salt dome with overhang. Each panel shows horizontal slices through the model. For the inversion we used responses at five frequencies from 1995 MT sites with 500 m spacing located inside the black dashed rectangle. Five percent noise was added to the simulated data.
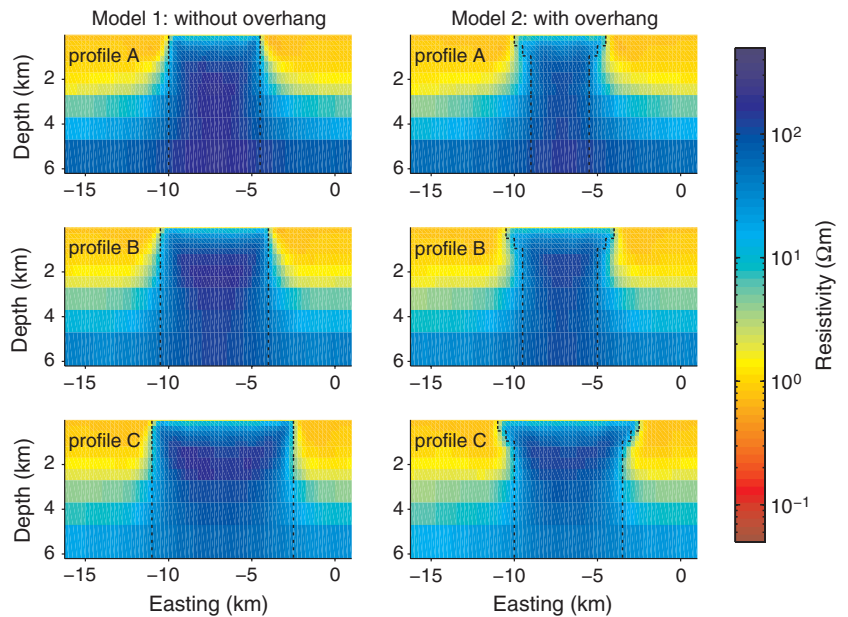

Figure 15. Comparison of the 3D inversion results for models without (left column) and with overhang (right column). Each panel presents a vertical cross section through the model. For the inversions, we used responses at five frequencies from 1995 MT sites with 500 m spacing. Fiver percent noise was added to the simulated data.
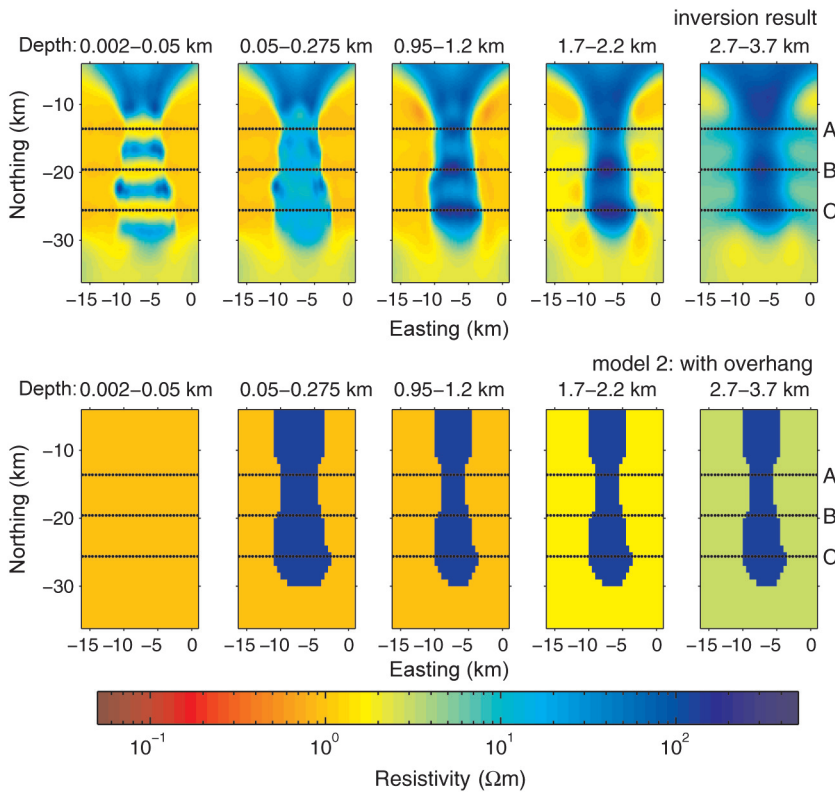
Figure 16. Comparison of the 3D inversion result (upper row) to the true model (lower row) of the salt dome with overhang. Each panel shows horizontal slices through the model. For the inversion, we used responses at five frequencies from 105 MT sites located along 3 profiles (horizontal dotted lines). Five percent noise was added to the simulated data.
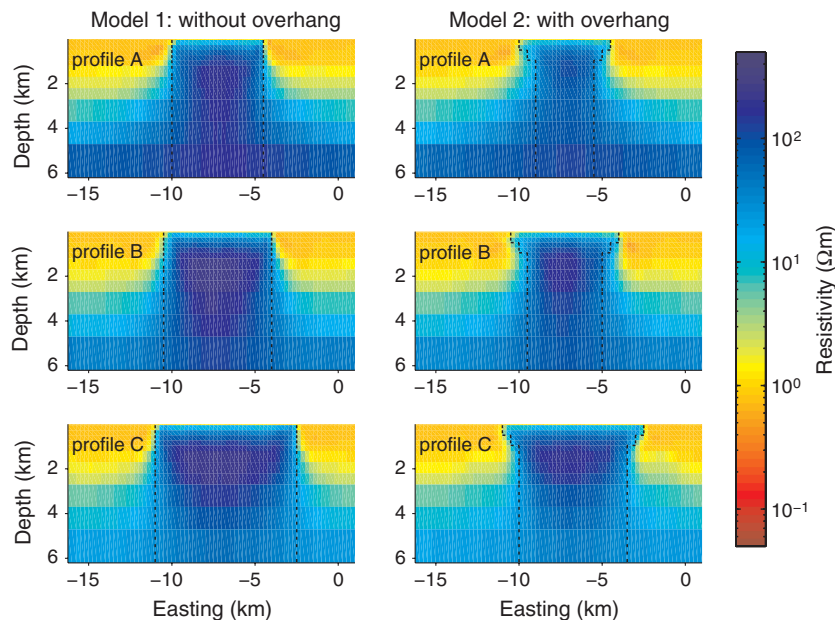

Figure 17. Comparison of the 3D inversion results for models without (left column) and with overhang (right column). Each panel presents a vertical cross section through the model. For the inversions, we used responses at five frequencies from 105 MT sites located along three profiles (see Figure 7). Five percent noise was added to the simulated data.

anomalies are recovered well. Presence of the salt overhang can be identified for profiles C and B, whereas for profile A it is difficult to see the overhang.

CONCLUSIONS

In this paper, we perform a salt dome overhang detectability study. For this, we first adjust our inversion approach to the specific problem of a resistive salt structure. We test various model parameterizations and regularization functionals and demonstrate on a relatively small-sized model of two adjacent blocks that a parametrization with logarithms of conductivities and a regularization functional based on the first-derivatives, rather than the Laplace operator, are the most suitable choices.

Comparing the responses for two salt dome models with and without overhang shows that MT is very sensitive to shallow salt structures. The anomalous responses due to the salt structures and the overhang are localized, nearly repeating the shape of the 3D anomaly. Hence, the responses are not influenced by other nearby structures and it is sufficient to place MT sites immediately in the vicinity of the anomaly. To resolve the salt structures dense MT site coverage over its flanks is advantageous. We apply our improved 3D MT inversion algorithm to simulated data. Our results demonstrate that structures like the salt dome are potentially resolved with 3D and profile MT data and a salt overhang may be resolved even with profile data only.

ACKNOWLEDGMENTS

REFERENCES

Avdeev, D. B., and A. D. Avdeeva, 2009, 3D magnetotelluric inversion using a limited-memory quasi-Newton optimization: Geophysics, **74**, no. 3, F45–F57, doi: 10.1190/1.3114023.

Avdeev, D. B., A. V. Kuvshinov, O. V. Pankratov, and G. A. Newman, 1997, High-performance three-dimensional electromagnetic modeling using modified Neumann series. Wide-band numerical solution and examples: Journal of Geomagnetism and Geoelectricity, **49**, no. 11–12, 1519–1539, doi: 10.5636/jgg.49.1519.

Avdeev, D. B., A. V. Kuvshinov, O. V. Pankratov, and G. A. Newman, 2002, Three-dimensional induction logging problems, Part I: An integral equation solution and model comparisons: Geophysics, **67**, 413–426, doi: 10.1190/1.1468601.

Avdeeva, A. D., and D. B. Avdeev, 2006, A limited-memory quasi-Newton inversion for 1D magnetotel-

lurics: Geophysics, **71**, no. 5, G191–G196, doi: 10.1190/1.2236381.

Constable, S. C., A. S. Orange, G. M. Hoversten, and H. F. Morrison, 1998, Marine magnetotellurics for petroleum exploration, Part I: A sea-floor equipment system: Geophysics, **63**, 816–825, doi: 10.1190/1.1444393.

Haber, E., 2005, Quasi-Newton methods for large-scale electromagnetic inverse problems: Inverse Problems, **21**, 305–323, doi: 10.1088/0266-5611/21/1/019.

Haber, E., U. Asher, and D. Oldenburg, 2000, On optimization techniques for solving nonlinear inverse problems: Inverse Problems, **16**, 1263–1280, doi: 10.1088/0266-5611/16/5/309.

Hoversten, G. M., S. C. Constable, and H. F. Morrison, 2000, Marine magnetotellurics for base-of-salt mapping: Gulf of Mexico field test at the Gemini structure: Geophysics, **65**, 1476–1488, doi: 10.1190/1.1444836.

Hoversten, G. M., H. F. Morrison, and S. C. Constable, 1998, Marine magnetotellurics for petroleum exploration, Part II: Numerical analysis of subsalt resolution: Geophysics, **63**, 826–840, doi: 10.1190/1.1444394.

Key, K., S. C. Constable, and C. Weiss, 2006, Mapping 3D salt using the 2D marine magnetotelluric method: Case study from Gemini Prospect, Gulf of Mexico: Geophysics, **71**, no. 1, B17–B27, doi: 10.1190/1.2168007.

Key, K., and C. Weiss, 2006, Adaptive finite-element modeling using unstructured grids: The 2D magnetotelluric example: Geophysics, **71**, no. 6, G291–G299, doi: 10.1190/1.2348091.

Mackie, R. L., and T. R. Madden, 1993, Three-dimensional magnetotelluric inversion using conjugate gradients: Geophysical Journal International, **115**, 215–229, doi: 10.1111/gji.1993.115.issue-1.

Mackie, R. L., J. T. Smith, and T. R. Madden, 1994, Three-dimensional electromagnetic modeling using finite difference equations: The magnetotelluric example: Radio Science, **29**, no. 4, 923–935, doi: 10.1029/94RS00326.

Moorkamp, M., B. Heincke, M. Jegen, A. W. Roberts, and R. W. Hobbs, 2011, A framework for 3-D joint inversion of MT, gravity and seismic refraction data: Geophysical Journal International, **184**, 477–493, doi: 10.1111/gji.2010.184.issue-1.

Newman, G. A., and D. L. Alumbaugh, 2000, Three-dimensional magnetotelluric inversion using non-linear conjugate gradients: Geophysical Journal International, **140**, 410–424, doi: 10.1046/j.1365-246x.2000.00007.x.

Newman, G. A., and P. T. Boggs, 2004, Solution accelerators for large-scale three-dimensional electromagnetic inverse problem: Inverse Problems, **20**, S151–S170, doi: 10.1088/0266-5611/20/6/S10.

Nocedal, J., and S. J. Wright, 1999, Numerical optimization: Springer-Verlag.

Ogilvie, J. S., and G. W. Purnell, 1996, Effects of salt-related mode conversions on subsalt prospecting: Geophysics, **61**, 331–348, doi: 10.1190/1.1443962.

Parker, R. L., 1994, Geophysical inverse theory: Princeton University Press.

Rodi, W., 1976, A technique for improving the accuracy of finite element solution for magnetotelluric data: Geophysical Journal of the Royal Astronomical Society, **44**, 483–506, doi: 10.1111/gji.1976.44.issue-2.

Sasaki, Y., 2004, Three-dimensional inversion of static-shifted magnetotelluric data: Earth, Planets and Space, **56**, no. 2, 239–248, doi: 10.1016/j.jappgeo.2008.02.002.

Siripunvaraporn, W., G. Egbert, Y. Lenbury, and M. Uyeshima, 2005, Three-dimensional magnetotelluric inversion: Data-space method: Physics of the Earth and Planetary Interiors, **150**, no. 1–3, 3–14, doi: 10.1016/j.pepi.2004.08.023.

Tikhonov, A. N., and V. Y. Arsenin, 1977, Solutions of ill-posed problems: Wiley-Interscience.

Wannamaker, P. E., 1991, Advances in three-dimensional magnetotelluric modeling using integral equations: Geophysics, **56**, 1716–1728, doi: 10.1190/1.1442984.

Zhdanov, M. S., and N. G. Golubev, 2003, Three-dimensional inversion of magnetotelluric data in complex geological structures: Australian Society of Exploration Geophysics, **20**, 550–553, doi: 10.1071/ASEG2003_3DEMab028.

Zhdanov, M. S., L. Wan, A. Gribenko, M. Cuma, K. Key, and S. Constable, 2009, Rigorous 3D inversion of marine magnetotelluric data in the area with complex bathymetry: 79th Annual International Meeting, SEG, Expanded Abstracts, 729–733.